Extensions of Goal-Oriented Error Estimation Methods to Simulations of Highly-Nonlinear Response of Shock-Loaded Elastomer-Reinforced Structures

David Fuentes, [1] David Littlefield, [2] J. Tinsley Oden, [3]
and Serge Prudhomme [4]

Institute for Computational Engineering and Sciences
The University of Texas at Austin
Austin, Texas 78712

Abstract

This paper describes extensions of goal-oriented methods for *a posteriori* error estimation and control of numerical approximation to a class of highly-nonlinear problems in computational solid mechanics. An updated Lagrangian formulation formulation of the dynamic, large-deformation response of structures composed of strain-rate-sensitive elastomers and elastoplastic materials is developed. To apply the theory of goal-oriented error estimation, a backward-in-time dual formulation of these problems is derived, and residual error estimators for meaningful quantities of interest are established. The target problem class is that of axisymmetric deformations of layered elastomer-reinforced shells-of-revolution subjected to shock loading. Extensive numerical results on solutions of representative problems are given. It is shown that extensions of the theory of goal-oriented error estimation can be developed and applied effectively to a class of highly-nonlinear, multi-physics problems in solid and structural mechanics.

Key words: nonlinear continuum mechanics, shock loading, goal-oriented error estimation, *a posteriori* error estimation, dual problem

---

[1] Graduate Research Assistant
[2] Research Scientist, ICES
[3] Director of ICES and Cockrell Family Regents Chair of Engineering
[4] Research Scientist, ICES

		Form Approved OMB No. 0704-0188

Report Documentation Page

1. REPORT DATE **27 JUN 2005**	2. REPORT TYPE	3. DATES COVERED **-**

4. TITLE AND SUBTITLE **Extensions of Goal-Oreinted Error Estimation Methods to Simulations of Highly-Nonlinear Response of Shock-Loaded Elastomer-Reinforced Structures**	5a. CONTRACT NUMBER
	5b. GRANT NUMBER
	5c. PROGRAM ELEMENT NUMBER
6. AUTHOR(S)	5d. PROJECT NUMBER
	5e. TASK NUMBER
	5f. WORK UNIT NUMBER
7. PERFORMING ORGANIZATION NAME(S) AND ADDRESS(ES) **Office of Naval Research,One Liberty Center,875 North Randolph Street Suite 1425,Arlington,VA,22203-1995**	8. PERFORMING ORGANIZATION REPORT NUMBER
9. SPONSORING/MONITORING AGENCY NAME(S) AND ADDRESS(ES)	10. SPONSOR/MONITOR'S ACRONYM(S)
	11. SPONSOR/MONITOR'S REPORT NUMBER(S)

12. DISTRIBUTION/AVAILABILITY STATEMENT
Approved for public release; distribution unlimited

13. SUPPLEMENTARY NOTES
The original document contains color images.

14. ABSTRACT
see report

15. SUBJECT TERMS

16. SECURITY CLASSIFICATION OF:			17. LIMITATION OF ABSTRACT	18. NUMBER OF PAGES **31**	19a. NAME OF RESPONSIBLE PERSON
a. REPORT **unclassified**	b. ABSTRACT **unclassified**	c. THIS PAGE **unclassified**			

1 Introduction

We revisit a subject addressed nearly a half-century ago by John Argyris: "Continua and Discontinua", where some of the early finite element approximations of a large class of nonlinear problems in continuum mechanics were presented [2]. Our goal here is to bring to the toolkit a new methodology for problems in nonlinear continuum mechanics: goal-oriented *a posteriori* error estimation for highly nonlinear dynamic simulations of the deformation of submerged bodies subjected to shock loading.

Methods for developing *a posteriori* estimates of finite element approximations of linear elliptic boundary-value problems first appeared in the literature in the late 1970's, beginning with the work of Ladevèze [12] for elasticity problems and of Babuška and Rheinboldt [3] on two-point boundary-value problems and followed in the early 1980's by extensions to elliptic problems on two- and three-dimensional domains [4,5,15]. Until the mid 1990's, except maybe the work of Gartland [10], virtually all of the methods of error estimation, an essential ingredient in mesh adaptation techniques, were applicable to global estimates of error in finite element approximations of linear boundary-value problems. A review of *a posteriori* error estimation can be found in the monograph of Ainsworth and Oden [1]. Global estimates for certain classes of nonlinear elliptic problems were contributed by Verfürth [23] see also [1]. More recently, techniques for developing *a posteriori* error estimates of so-called quantities-of-interest which are functionals of solutions of linear PDE's, were presented by Oden and Prudhomme [16,17] and Becker and Rannacher (e.g. [6]). These techniques employ optimal control strategies and involve the solution of a dual problem in which the quantity of interest appears as data. A variety of applications of these ideas have appeared since 2000 (e.g. [19–22]). The paper of Becker and Rannacher [6] appearing in 2001 extended the dual-based theory of error estimation to nonlinear boundary- and initial-value problems, and the paper of Oden and Prudhomme [17] extended the theory further to cover estimation of both modeling and approximation error in 2002. Further extension of this work to multi-scale modeling methods is described in a recent report [18].

While the developments to date provide an abstract mathematical framework for error estimation in highly nonlinear problems, no applications to important problems in nonlinear continuum mechanics appear to have been made, owing to the inherent complexities in such problems. To capture features of the nonlinear dynamics of solid bodies and structures under shock loading involves a host of complicated features and has been the focus of research in computational solid mechanics for many decades (see [14] or the more recent treatise [7]). The analysis of the evaluation of approximation error of quantities of interest in such applications involves solving first a forward-in-time problem for the system response, and then a backward-in-time problem for

the dual solution associated with the particular quantity of interest.

In the present investigation, *a posteriori* error estimates for key quantities of interest are derived for a class of complex and highly-nonlinear problems in computational solid mechanics: the dynamical behavior of a heterogeneous, layered shells subjected to shock loading. The models considered here involve axisymmetric deformations of thick bodies-of-revolution undergoing very high strains and strain rates, and large elastic and inelastic deformations. The target applications of the methods developed in this investigation is the dynamical behavior of elastomer-reinforced steel shells subjected to high-intensity shock loading.

Following the introduction, the underlying theory of *a posteriori* error estimation is given in Section 2. The formulation of a continuum model of the problem is given in Section 3. Here a framework suitable for goal-oriented error estimation is presented and algorithms used to compute the solution of the discretized space and time problem are established. Section 4 presents the equations of goal-oriented error estimation and the particular solution technique used. The method of assessing the fidelity of the solution is also discussed. The geometry and data of the target application problems are given in Section 5 and Section 6 presents the constitutive equations used in the computational model. Detailed numerical results are presented and discussed in Section 7. Concluding comments are collected in Section 8.

2   Goal-Oriented *A Posteriori* Error Estimation and Control

The theory of goal-oriented error estimation and control can be described in terms of the abstract problem,

$$
\boxed{
\begin{aligned}
&\text{Find } u \in \mathcal{V} \text{ such that} \\
&\quad B(u; v) = F(v) \quad \forall v \in \mathcal{V}
\end{aligned}
}
\tag{1}
$$

where $B(\cdot, \cdot)$ is a semilinear form, nonlinear in the first entry, v is a test vector, $F(\cdot)$ a linear functional, and $\mathcal{V}$ is the space of admissible solutions, here a Banach space with norm $\| \cdot \|_{\mathcal{V}}$. Of interest is the value of a functional $Q : \mathcal{V} \to \mathbb{R}$ at solutions u to (1); the quantity of interest. The problem of determining $Q(u) = \inf\{Q(v) : v \in \mathcal{V}\}$ subject to (1) is an optimal control problem characterized by the pair of equations:

$$
\boxed{
\begin{aligned}
&\text{Find } (u, p) \in \mathcal{V} \times \mathcal{V} \text{ such that} \\
&\quad B(u; v) = F(v) \quad \forall v \in \mathcal{V} \\
&\quad B'(u; w, p) = Q(u; w) \quad \forall w \in \mathcal{V}
\end{aligned}
}
\tag{2}
$$

3

Here

$$B'(u; w, p) = \lim_{\theta \to 0} \frac{1}{\theta} \left[B(u + \theta w; p) - B(u; p) \right]$$
$$Q'(u; w) = \lim_{\theta \to 0} \frac{1}{\theta} \left[Q(u + \theta w) - Q(u) \right] \tag{3}$$

Problem $(2)_1$ is the dual problem associated with the quantity of interest Q and the primal problem (1) (or $(2)_2$). The dual problem is thus linear in p, but coupled to the possibly nonlinear primal problem.

We next consider a family $\{\mathcal{V}^h\}$ of finite-dimensional subspaces of $\mathcal{V}$ with everywhere dense union

$$\bigcup_{h \to 0} \mathcal{V}^h$$

generated, for example, through finite element approximations of functions (vectors) in $\mathcal{V}$. The Galerkin approximation of (2) on a subspace $\mathcal{V}^h$ is then

$$
\boxed{
\begin{aligned}
&\text{Find } (u^h, p^h) \in \mathcal{V}^h \times \mathcal{V}^h \text{ such that} \\
&\quad B(u^h; v^h) = F(v^h) \qquad \forall v^h \in \mathcal{V}^h \\
&\quad B'(u^h; w^h, p^h) = Q(u^h; w^h) \qquad \forall w^h \in \mathcal{V}^h
\end{aligned}
}
\tag{4}
$$

The goal is to estimate the approximation error $\mathcal{E}^h$ in the target quantity of interest Q. In [17] (see also [6]), it is shown that to within terms of quadratic order or higher in the error components $e^h = u - u^h$ and $\varepsilon^h = p - p^h$, the (*a posteriori*) error in the quantity of interest is

$$\mathcal{E}^h = Q(u) - Q(u^h) \approx \mathcal{R}(u^h, p) \tag{5}$$

where $\mathcal{R}(u^h, \cdot)$ is the residual functional,

$$\mathcal{R}(u^h; p) = F(p) - B(u^h; p) \tag{6}$$

We note that the Galerkin approximation p^h of p satisfies the orthogonality condition,

$$\mathcal{R}(u^h; p^h) = 0 \tag{7}$$

Various *goal-oriented algorithms* may be constructed for systematically reducing the error $\mathcal{E}^h$ [19–21]. Our objective is to formulate the field equations of nonlinear continuum mechanics so that they conform to the structure of (2), and to then develop goal-oriented methods for *a posteriori* error estimation and control of models simulating the nonlinear dynamics of layered shell-like structures.

4

3 Variational Formulation

Basic elements of the formulation and much of our notation are standard. We use an updated Lagrange formulation of the field equations of nonlinear continuum mechanics.

3.1 Weak Form of the Primal Problem

The forward (primal) problem for an updated Lagrange formulation of the equations governing the motion of a material body is characterized as follows:

$$
\begin{array}{|l|}
\hline
\text{Find } (\mathbf{u}, \mathbf{v}) \in \mathcal{V} \text{ such that} \\
\quad B((\mathbf{u}, \mathbf{v}); (\mathbf{z}, \mathbf{w})) = F((\mathbf{z}, \mathbf{w})) \qquad \forall (\mathbf{z}, \mathbf{w}) \in \mathcal{V} \\
\hline
\end{array}
\tag{8}
$$

Here $\mathcal{V} = \mathcal{Z} \times \mathcal{W}$ is a product space of admissible displacement-velocity pairs and $B(\cdot; \cdot)$ and $F(\cdot)$ are the semilinear and linear forms:

$$
B((\mathbf{u}, \mathbf{v}); (\mathbf{z}, \mathbf{w})) =
$$
$$
\int_0^T \int_{\Omega_t} \left(\rho \frac{d\mathbf{v}}{dt} \cdot \mathbf{w} + \rho \frac{d\mathbf{u}}{dt} \cdot \mathbf{z} - \rho \mathbf{v} \cdot \mathbf{z} + \boldsymbol{\sigma} : \nabla_x \mathbf{w} \right) dx dt
$$
$$
+ \int_{\Omega_0} \left(\rho_0 \mathbf{v}(\mathbf{X}, 0) \cdot \mathbf{w}(\mathbf{X}, 0) + \rho_0 \mathbf{u}(\mathbf{X}, 0) \cdot \mathbf{z}(\mathbf{X}, 0) \right) dX
\tag{9}
$$

$$
F((\mathbf{z}, \mathbf{w})) =
$$
$$
\int_0^T \int_{\Gamma_t^N} \mathbf{g} \cdot \mathbf{w} \, dA dt + \int_{\Omega_0} \left[\rho_0 \mathbf{v}_0(\mathbf{X}) \cdot \mathbf{w}(\mathbf{X}, 0) + \rho_0 \mathbf{u}_0(\mathbf{X}) \cdot \mathbf{z}(\mathbf{X}, 0) \right] dX
\tag{10}
$$

Here we ignore body forces and consider the motion over a time interval $[0, T]$ of a material body occupying a current configuration $\Omega_t \subset \mathbb{R}$ at time t, Ω_0 being the reference configuration. The energy equation is not considered in its weak form. In (9) and (10),

$$
\rho = \rho(\mathbf{x}, t) \text{ is the current mass density}
$$
$$
\mathbf{x} \text{ being the spatial position}
$$
$$
\text{of material particles that were located}
$$
$$
\text{at position } \mathbf{X} \text{ in the reference configuration}
$$
$$
\mathbf{v} = \mathbf{v}(\mathbf{x}, t) \text{ the velocity field}
$$
$$
\mathbf{u} = \mathbf{u}(\mathbf{x}, t) \text{ the displacement field}
$$
$$
\boldsymbol{\sigma} = \boldsymbol{\sigma}(\mathbf{x}, t) \text{ the Cauchy stress tensor}
$$
$$
\nabla_x = \mathbf{e}_i \frac{\partial}{\partial x_i} \text{ the spatial gradient}
$$

3.2   Time-Discretized Formulation
The governing equations with initial conditions for the Updated Lagrangian formulation are presented below

$$\rho J = \rho_0$$
$$\rho(\mathbf{X}, 0) = \rho_0(\mathbf{X})$$
$$\int_{\Omega_t} \rho \frac{d\mathbf{v}}{dt} \cdot \mathbf{w} + \boldsymbol{\sigma} : \nabla_x \mathbf{w} \, dx = \int_{\Gamma_t^N} \mathbf{g} \cdot \mathbf{w} \, dA$$
$$\mathbf{v}(\mathbf{X}, 0) = \mathbf{v}_0(\mathbf{X})$$
$$\frac{d\mathbf{u}}{dt} = \mathbf{v}$$
$$\mathbf{u}(\mathbf{X}, 0) = \mathbf{u}_0(\mathbf{X})$$
$$\rho \frac{de}{dt} = \boldsymbol{\sigma} : \mathbf{D}$$
$$e(\mathbf{X}, 0) = e_0(\mathbf{X})$$

Here the strong forms of the mass equation, the velocity-displacement relation, and conservation of energy are assumed. Conservation of momentum is the only equation considered in its weak form.

The time interval $[0, T]$ is decomposed into subintervals $[t^n, t^{n+1}]$ where the time step

$$\Delta t = \frac{t^{n+1} - t^n}{2} \qquad t^{n+\frac{1}{2}} \equiv \frac{1}{2}(t^{n+1} + t^n)$$

is determined by the Courant condition. The algorithm used for advancing the velocity and displacement fields in time is based on the following finite difference scheme for the acceleration

$$\left. \frac{d\mathbf{v}}{dt} \right|_{t=t^n} \approx \frac{\mathbf{v}^{n+\frac{1}{2}} - \mathbf{v}^{n-\frac{1}{2}}}{t^{n+\frac{1}{2}} - t^{n-\frac{1}{2}}}$$

A *leap frog* method is used: the velocities and displacements are computed half a time step apart. The time-discrete momentum equation is then of the form

$$\int_{\Omega_{t^n}} \rho^n \mathbf{v}^{n+\frac{1}{2}} \cdot \mathbf{w}^n dx = \int_{\Omega_{t^n}} \rho^n \mathbf{v}^{n-\frac{1}{2}} \cdot \mathbf{w}^n dx$$
$$+ (t^{n+\frac{1}{2}} - t^{n-\frac{1}{2}}) \left[\int_{\Gamma_{t^n}^N} \mathbf{g}^n \cdot \mathbf{w}^n \, dA - \int_{\Omega_{t^n}} \boldsymbol{\sigma}^n : \nabla_x \mathbf{w}^n \, dx \right] \tag{11}$$

where ρ^n is calculated from the mass equation

$$\rho^n J^n = \rho_0(\mathbf{X})$$

The displacement is updated in a similar manner as

$$\mathbf{u}^{n+1} = \mathbf{u}^n + (t^{n+1} - t^n)\mathbf{v}^{n+\frac{1}{2}} \tag{12}$$

While the energy equation is approximated point-wise using the following finite difference scheme

$$\rho^n e^{n+1} = \rho^n e^n + (t^{n+1} - t^n)\boldsymbol{\sigma}^n : \mathbf{D}^{n-\frac{1}{2}} \tag{13}$$

and is only used to update the yield stress of the materials. As the name indicates, during the Lagrangian step the mesh is moved with the material.

Algorithm 1 explicit time algorithm for velocity and displacement
---
    use initial conditions to obtain $\mathbf{v}^{\frac{1}{2}}$ and $\mathbf{u}^0$
    for $n = 1$ to $ncycle$ **do**
        determine Δt from Courant condition
        update stress $\boldsymbol{\sigma}^n = \boldsymbol{\sigma}^n(\mathbf{u}^n, \mathbf{v}^{n-\frac{1}{2}}, e^n)$
        use (11) to compute $\mathbf{v}^{n+\frac{1}{2}}$
        update energy using (13)
        use (12) to compute $\mathbf{u}^{n+1}$
    end for

The specific applications of this formulation to be considered in Section 5, 6, and 7 also involve contact problems encountered in layered structures in which layers are not bound together but merely are in physical contact in the reference configuration.

The layered shells are therefore modeled with a sliding interface between the layers, with the interface treated as a contact region. The standard treatment of contact is to assume that the bodies in contact cannot overlap and that the tractions of the surfaces of the contact region satisfy momentum conservation at the interface. In the computations, these two conditions impose another set of nonlinear equations to be coupled to the updated Lagrangian equations of motion. A comprehensive treatment of contact and implementation may be found in Belytschko [7].

The contact algorithm does not alter the dual formulation. From the view point of the elastomeric material, in which the dual solution was computed, the contact region is merely a different set of traction boundary conditions on the Neumann boundary.

4 The Dual Variational Formulation

There are two distinct sources of error in our discretized primal problem. One source arises from the finite difference approximation of the time derivatives and the second source of error from the finite element approximation of the solution. This analysis is primarily concerned with the latter. In the following sections our problem will be placed in a suitable framework for goal-oriented error estimation as developed by Oden and Prudhomme [17]. The dual problem

7

to our primal problem will be established and discretized. Treatment of error estimation is restricted entirely to the elastomeric layer of the shell structure. Consider as the primal problem the updated Lagrangian equations formulated on the elastomer layer, see Figure 2. From this point of view, the remainder of the computational simulation will merely serve to prescribe boundary conditions.

4.1 Dual Problem Procedures for deriving the dual problem has been presented in Oden and Prudhomme [16,17] and Becker and Rannacher [6]. Consider a particular quantity of interest characterized by a functional Q, defined on $\mathcal{V}$:

$$Q((\mathbf{u}, \mathbf{v})) = \int_{\Omega_T} K(\mathbf{x}) u_z \, dx \tag{14}$$

where $K(\mathbf{x})$ is a kernel function on the deformed region underneath the shock loading material in the final configuration, Ω_T. The kernel function is defined such that the quantity of interest represents a local average of the vertical displacement u_z over a sub-domain of Ω_T. The relevance of this quantity of interest will become clear when the target problem is presented in Section 5.

Following [17], the dual problem of (8) is given as follows

$$
\boxed{
\begin{array}{l}
\text{Find } (\mathbf{p}, \mathbf{q}) \in \mathcal{V} \text{ such that} \\
\quad B'((\mathbf{u}, \mathbf{v}); (\mathbf{z}, \mathbf{w}), (\mathbf{p}, \mathbf{q})) = Q'((\mathbf{u}, \mathbf{v}); (\mathbf{z}, \mathbf{w})) \quad \forall (\mathbf{z}, \mathbf{w}) \in \mathcal{V}
\end{array}
}
\tag{15}
$$

where B' and Q' are the derivatives of B and Q, respectively, i.e.

$$B'((\mathbf{u}, \mathbf{v}); (\mathbf{z}, \mathbf{w}), (\mathbf{p}, \mathbf{q})) \equiv$$
$$\lim_{\theta \to 0} \frac{1}{\theta} \left[B((\mathbf{u}, \mathbf{v}) + \theta(\mathbf{z}, \mathbf{w}); (\mathbf{p}, \mathbf{q})) - B((\mathbf{u}, \mathbf{v}); (\mathbf{p}, \mathbf{q})) \right]$$

and

$$Q'((\mathbf{u}, \mathbf{v}); (\mathbf{z}, \mathbf{w})) \equiv \lim_{\theta \to 0} \frac{1}{\theta} \left[Q((\mathbf{u}, \mathbf{v}) + \theta(\mathbf{z}, \mathbf{w})) - Q((\mathbf{u}, \mathbf{v})) \right]$$

For the quantity of interest particular to this problem

$$Q'((\mathbf{u}, \mathbf{v}); (\mathbf{z}, \mathbf{w})) = \int_{\Omega_T} K(x) z_z(x) dx$$

Applying the definition of B' to our semi-linear form

$$B'((\mathbf{u}, \mathbf{v}); (\mathbf{z}, \mathbf{w}), (\mathbf{p}, \mathbf{q})) =$$
$$\int_0^T \int_{\Omega_t} (\rho \frac{d\mathbf{w}}{dt} \cdot \mathbf{q} + \nabla_x \mathbf{q} : \delta \boldsymbol{\sigma}^u : \nabla_x \mathbf{z} + \nabla_x \mathbf{p} : \delta \boldsymbol{\sigma}^v : \nabla_x \mathbf{w} - \rho \mathbf{w} \cdot \mathbf{p} + \rho \frac{d\mathbf{z}}{dt} \cdot \mathbf{p}) \, dx dt$$
$$+ \int_{\Omega_o} (\rho_o \mathbf{w}(\mathbf{X}, 0) \cdot \mathbf{q}(\mathbf{X}, 0) + \rho_o \mathbf{z}(\mathbf{X}, 0) \cdot \mathbf{p}(\mathbf{X}, 0)) \, dX$$

8

Where $\delta\boldsymbol{\sigma}^v$ and $\delta\boldsymbol{\sigma}^u$ are obtained from the Taylor-expansions of the Cauchy stress:

$$\boldsymbol{\sigma}_{ij}(\nabla_x\mathbf{u} + \theta\nabla_x\mathbf{z}, \nabla_x\mathbf{v} + \theta\nabla_x\mathbf{w}) = \boldsymbol{\sigma}_{ij}(\nabla_x\mathbf{u}, \nabla_x\mathbf{v}) + \theta\frac{\partial\boldsymbol{\sigma}_{ij}}{\partial(\mathbf{u}_{m,n})}\mathbf{z}_{m,n}$$
$$+ \theta\frac{\partial\boldsymbol{\sigma}_{ij}}{\partial(\mathbf{v}_{m,n})}\mathbf{w}_{m,n} + \mathcal{O}(\theta^2)$$

with

$$\delta\boldsymbol{\sigma}^u_{ijmn} \equiv \frac{\partial\boldsymbol{\sigma}_{ij}}{\partial(\mathbf{u}_{m,n})} \qquad \delta\boldsymbol{\sigma}^v_{ijmn} \equiv \frac{\partial\boldsymbol{\sigma}_{ij}}{\partial(\mathbf{v}_{m,n})}$$

The explicit form of B' shows that the constitutive equations for the materials are intimately tied to the error estimate calculations.

Integrating by parts to transfer the time derivatives from the test functions, $(\mathbf{z}, \mathbf{w})$, to the influence functions, $(\mathbf{p}, \mathbf{q})$, the derivative of the semi-linear form becomes

$$B'((\mathbf{u}, \mathbf{v}); (\mathbf{z}, \mathbf{w}), (\mathbf{p}, \mathbf{q})) =$$
$$\int_0^T \int_{\Omega_t} \left(-\rho\mathbf{w}\cdot\frac{d\mathbf{q}}{dt} - \rho\mathbf{z}\cdot\frac{d\mathbf{p}}{dt} + \nabla_x\mathbf{q} : \delta\boldsymbol{\sigma}^u : \nabla_x\mathbf{z} + \nabla_x\mathbf{p} : \delta\boldsymbol{\sigma}^v : \nabla_x\mathbf{w} - \rho\mathbf{w}\cdot\mathbf{p}\right) dxdt$$
$$+ \int_{\Omega_T} \left(\rho\mathbf{w}(\mathbf{x}, T)\cdot\mathbf{q}(\mathbf{x}, T) + \rho\mathbf{z}(\mathbf{x}, T)\cdot\mathbf{p}(\mathbf{x}, T)\right) dx$$

$$(16)$$

From (16), it is seen that the initial conditions of the dual problem involve initial conditions of the influence functions at time $t = T$. This means that data of the influence functions must be known at time T and the influence functions are propagated backwards in time. This shows that any algorithm for computing the error in quantities of interest requires that the primal problem is first solved forward in time from 0 to T and the dual problem from T to 0; i.e. the states of the primal problem at all times in $[0, T]$ must be available to solve the dual problem.

4.2 Time discretization of dual problem For appropriately chosen test functions the dual problem may be written as two coupled first-order PDE's with conditions given at the final time:

$$\int_{\Omega_t} \left(\rho\mathbf{w}\cdot\frac{d\mathbf{q}}{dt} + \nabla_x\mathbf{p} : \delta\boldsymbol{\sigma}^v : \nabla_x\mathbf{w} + \rho\mathbf{w}\cdot\mathbf{p}\right) dx = 0$$
$$\mathbf{q}(\mathbf{x}, T) = 0$$
$$\int_{\Omega_t} \left(\nabla_x\mathbf{q} : \delta\boldsymbol{\sigma}^u : \nabla_x\mathbf{z} - \rho\mathbf{z}\cdot\frac{d\mathbf{p}}{dt}\right) dx = 0$$
$$p_1(\mathbf{x}, T) = p_2(\mathbf{x}, T) = 0, \qquad p_3(\mathbf{x}, T) = \frac{K(\mathbf{x})}{\rho}$$

$$(17)$$

The following time-implicit algorithm is implemented to reduce the amount of data needed to be stored while managing the results of the forward problem in coefficients of the dual problem at many time instances. Note that the time index has been switched from 'n' to 'k' to emphasize the time step difference between the explicit primal problem and the implicit dual problem.

Derivatives of the influence functions are approximated as

$$\frac{d\mathbf{q}}{dt}\bigg|_{t=t^{k-\frac{1}{2}}} \approx \frac{\mathbf{q}^k - \mathbf{q}^{k-1}}{t^k - t^{k-1}}$$

$$\frac{d\mathbf{p}}{dt}\bigg|_{t=t^{k-\frac{1}{2}}} \approx \frac{\mathbf{p}^k - \mathbf{p}^{k-1}}{t^k - t^{k-1}}$$

Thus, the time discretized dual problem may be written as

$$\int_{\Omega_{t^{k-\frac{1}{2}}}} \left(\nabla_x \mathbf{q}^{k-\frac{1}{2}} : (\delta\boldsymbol{\sigma}^u)^{k-\frac{1}{2}} : \nabla_x \mathbf{z}^{k-\frac{1}{2}} - \rho^{k-\frac{1}{2}} \mathbf{z}^{k-\frac{1}{2}} \cdot \frac{\mathbf{p}^k - \mathbf{p}^{k-1}}{t^k - t^{k-1}} \right) dx = 0 \quad (18)$$

$$\int_{\Omega_{t^{k-\frac{1}{2}}}} \left(\rho^{k-\frac{1}{2}} \mathbf{w}^{k-\frac{1}{2}} \cdot \frac{\mathbf{q}^k - \mathbf{q}^{k-1}}{t^k - t^{k-1}} + \rho^{k-\frac{1}{2}} \mathbf{w}^{k-\frac{1}{2}} \cdot \mathbf{p}^{k-\frac{1}{2}} \right) dx +$$
$$\int_{\Omega_{t^{k-\frac{1}{2}}}} \nabla_x \mathbf{p}^{k-\frac{1}{2}} : (\delta\boldsymbol{\sigma}^v)^{k-\frac{1}{2}} : \nabla_x \mathbf{w}^{k-\frac{1}{2}} \, dx = 0 \qquad (19)$$

where

$$\mathbf{p}^{k-\frac{1}{2}} \equiv \frac{\mathbf{p}^{k-1} + \mathbf{p}^k}{2}$$

$$\mathbf{q}^{k-\frac{1}{2}} \equiv \frac{\mathbf{q}^{k-1} + \mathbf{q}^k}{2}$$

The following is the pseudo-code used to implement the dual problem.

Algorithm 2 implicit time algorithm for influence functions
---
   when computing primal problem save:
      $\mathbf{u}^{k-\frac{1}{2}}$, $(\delta\boldsymbol{\sigma}^u)^{k-\frac{1}{2}}$, $(\delta\boldsymbol{\sigma}^v)^{k-\frac{1}{2}}$, $\mathbf{z}^{k-\frac{1}{2}}$, $\mathbf{w}^{k-\frac{1}{2}}$, and t^k for $k = 2, 3, ..., K_f$
   use final conditions to obtain $\mathbf{q}^{K_f}$ and $\mathbf{p}^{K_f}$, where $t^{K_f} = T$
   for $k = K_f$ to 2 by -1 **do**
     solve *linear* system of equations resulting from (18) and (19)
        to compute $\mathbf{q}^{k-1}$ and $\mathbf{p}^{k-1}$
   end for

4.3   ***A Posteriori Error Estimation and Residual Based Refinement*** Errors in the quantity of interest may be quantified by computation of the residual [17]. The residual is defined as

$$\mathcal{R}((\mathbf{u}^h, \mathbf{v}^h); (\mathbf{z}, \mathbf{w})) \equiv F((\mathbf{z}, \mathbf{w})) - B((\mathbf{u}^h, \mathbf{v}^h); (\mathbf{z}, \mathbf{w}))$$

and the error in the quantity of interest is approximated by

$$Q((\mathbf{u}, \mathbf{v})) - Q((\mathbf{u}^h, \mathbf{v}^h)) \approx \mathcal{R}((\mathbf{u}^{h_1}, \mathbf{v}^{h_1}); (\mathbf{p}, \mathbf{q}))$$
$$\approx \mathcal{R}((\mathbf{u}^{h_1}, \mathbf{v}^{h_1}); (\mathbf{p}^{h_2}, \mathbf{q}^{h_2})) \tag{20}$$

where $(\mathbf{u}^h, \mathbf{v}^h)$ is the computed solution. For these calculations, bilinear shape functions are used for the primal solution, $(\mathbf{u}^{h_1}, \mathbf{v}^{h_1})$, and second order serendipity elements are used for the dual solution, $(\mathbf{p}^{h_2}, \mathbf{q}^{h_2})$. Note that using bilinear shape functions for both the dual and primal solution would result in a residual of zero due to the Galerkin orthogonality property.

5 Application to Shock Loaded Layered Shell

The geometry of the problem of interest is given in Figures 2, 3, and 4. A shock-like pressure loading is applied normal to the entire outside surface of the shell. The pressure loading data is obtained from an independent simulation. The time evolution of the pressure loading at various distances from the centerline along the shell is given in Figure 1; the time evolution of the pressure at radii not shown may be taken as the linear interpolant.
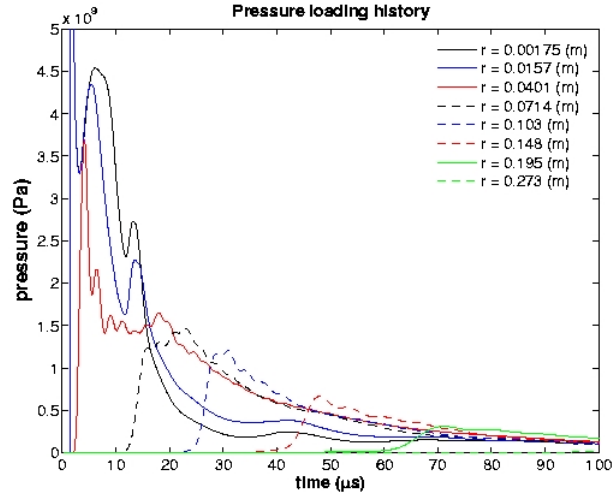
Figure 1. Time evolution of pressure loading on shell structure.

Three distinct configurations of the shell are considered. In the first configuration, shown in Figure 2, the shell is composed of two layers: the outer layer is steel and the inner layer is the elastomeric material. As indicated in Figure 1, the pressure load is applied normal to the entire outer surface of the steel. The intensity of the loading is largest within a radius of $r = 3.49$cm from the centerline. The thickness of the steel is $t_{steel} = 1.27$cm and the thickness of the elastomer is $t_{elastomer} = 2.54$cm. Two interface conditions between the steel and elastomer are considered: perfectly bonded and frictionless sliding.

11

In the second configuration, the layers are reversed, the outer layer being now made of elastomer and the inner layer of steel (see Figure 3). The pressure load is applied to the outer surface of the elastomer. Again, the thickness of the steel is $t_{steel} = 1.27$cm and the thickness of the elastomer is $t_{elastomer} = 2.54$cm. Similar to the first configuration, perfectly bonded and frictionless sliding interface conditions are considered.
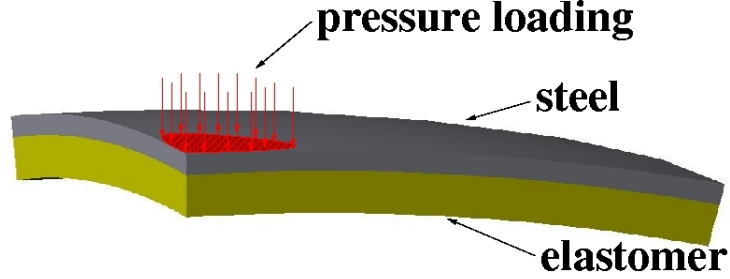

Figure 2. Geometry of the problem of interest for the first configuration of the layered shell.
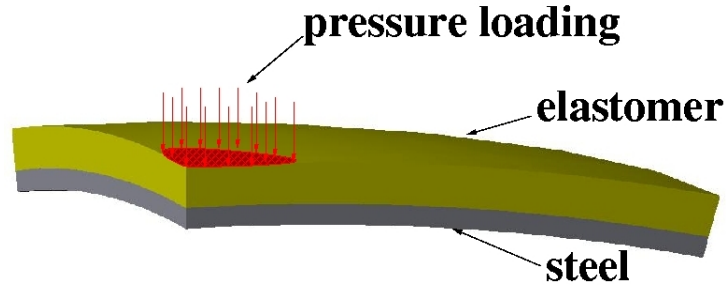
Figure 3. Geometry of the problem of interest for the second configuration of the layered shell.

The final configuration considered is the base configuration, the elastomer is removed and the shell is composed entirely of steel (see Figure 4). The thickness of the steel is $t_{steel} = 1.27$cm. This configuration will be used as the basis for comparison of the effect of the elastomeric layer.
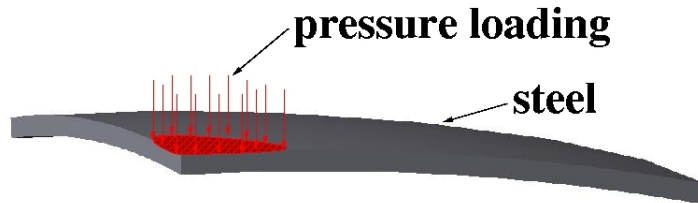
Figure 4. Base configuration of shell.

All geometries are assumed to have a rotational axis of symmetry as illustrated. The problems are modeled with a Lagrangian mesh throughout the domain. The updated Lagrangian equations are solved throughout the mesh.

Among quantities of interest are those that indicate the effectiveness of the elastomeric layer as a reinforcement of the steel structure. Therefore, the quantity of interest in this investigation has been defined (14) as the displacement of a region of the layered shell under the shock loading source. This quantity will be used as a measure of the damage inflicted by the shock loading.

6 Constitutive Equations

The Cauchy stress for each material is decomposed into its dilatational and deviatoric components

$$\sigma = -p\mathbf{I} + \mathbf{S}, \quad s_{ij} = \sigma_{ij} + p\delta_{ij}$$

where p denotes the mechanical pressure. Thermodynamic equilibrium is assumed so that the mechanical pressure equals the thermodynamic pressure provided by an equation of state.

The shock conditions suggest that an equation of state based on Hugoniot data is well suited for this problem. Thus, the steel is modeled as a hypoelastic-plastic material using a Mie-Gruneisen equation of state to model the pressure.

$$
\begin{aligned}
p &= p_h + \rho_o \Gamma_o (e - e_h) \\
p_h &= p_o + \frac{\rho_o C_o^2 \eta}{(1 - s\eta)^2}, \qquad \eta = 1 - \frac{\rho_o}{\rho} \\
e_h &= e_o + \frac{\eta}{2\rho_o}(p_h + p_o)
\end{aligned}
\tag{21}
$$

where p_h is the Hugoniot pressure, e_h is the Hugoniot energy; Γ_o is the Gruneisen gamma, C_o is the reference sound speed, and s is the slope of the particle velocity-shock velocity curve.

The deviatoric stress, $\mathbf{S}$, is also obtained from the equation of state. The bulk modulus is proportional to the partial derivative of pressure with respect to density at constant internal energy:

$$K = \rho \left(\frac{\partial p}{\partial \rho} \right)_e$$

The Poisson ratio, ν, and the bulk modulus, K, are used to formulate the deviatoric component of the stress:

$$G = \frac{3K(1 - 2\nu)}{2(1 + \nu)} \qquad \mathbf{S}^{\nabla J} = G\mathbf{D}_{dev}$$

where $\mathbf{S}^{\nabla J}$ is the Jaumman rate of the deviatoric stress tensor and G is the shear modulus.

Plasticity is modeled following classical $J2$ flow theory where the yield stress, σ_y, is obtained from a Johnson-Cook plasticity model. All material data parameters are given in Tables 1 and 2.

$$\sigma_y = \left(A + Be_p^n\right)\left(1 + C\ln(\dot{e}_p)\right)\left(1 - T_*^m\right)$$

Table 1. Plasticity parameters for steel

A (Pa)	B	n	c	m	T_* (K)
0.7922×10^9	0.676	0.26	0.014	1.03	1793.0

Here e_p^n is the effective plastic strain, $\dot{e}_p$ is the effective plastic strain rate, and T_* is the effective temperature defined in terms of the melting temperature, ambient temperature, and Hugoniot temperature; T_m, T_{ref}, and T_h, respectively.

$$T_* = \frac{T - T_{ref}}{T_m - T_{ref}}, \qquad T = T_h + \frac{e - e_h}{c_v}$$

Based on the experiments performed at UCSD [13], under shock loading conditions the deviatoric component of stress in the elastomer is insignificant compared to the pressure. Therefore, the elastomer has been modeled hydrodynamically for these simulations, $\mathbf{S} = \mathbf{0}$. A Mie-Gruneisen equation of state is assumed, equation (21). The parameters C_o and s of the Mie-Gruneisen equation of state are obtained from a graph of the data shown in Figure 5. The rest of the Mie-Gruneisen parameters are given in Table 2,

Table 2. Mie-Gruneisen EOS parameters

mat	ρ_o ($\frac{\text{kg}}{\text{m}^3}$)	$C_o(\frac{\text{m}}{\text{s}})$	s	Γ_o	$c_v(\frac{\text{J}}{\text{kg K}})$	ν
steel	7.85×10^3	4.5×10^3	1.49	2.17	4.48×10^2	0.3
elastomer	1.07×10^3	2.503×10^3	2.05	1.55	1.173×10^3	0.4998

Assuming a hydrodynamic state of stress for elastomer,

$$\sigma_{ij} = -p\delta_{ij}$$

and neglecting the dependence on $\nabla_x \mathbf{v}$, the stress variation in the dual problem becomes

$$\delta\boldsymbol{\sigma}_{ijmn}^v = 0$$
$$\delta\boldsymbol{\sigma}_{ijmn}^u = \frac{\partial\boldsymbol{\sigma}_{ij}}{\partial(\mathbf{u}_{m,n})} = \frac{\partial p}{\partial(\mathbf{u}_{m,n})}\delta_{ij} = \frac{\partial p}{\partial\rho}\cdot\frac{\rho_o}{J^2}\cdot C_{mn}\delta_{ij}$$
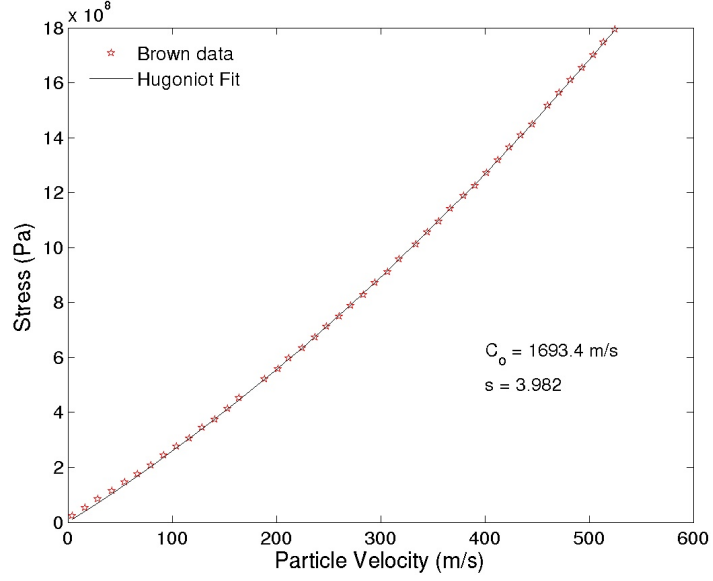
14

Figure 5. Elastomer Data

where for an axisymmetric problem

$$
\begin{aligned}
C_{11} &= (F_{11}\ F_{22}\ u_{3,3}\ F_{33} - F_{21}\ F_{12}\ u_{3,3}\ F_{33} + F_{11}\ F_{22} - F_{21}\ F_{12})\ u_{2,2} \\
&\quad + F_{11} + F_{11}\ u_{3,3}\ F_{33} \\
C_{22} &= (F_{11}\ F_{22}\ u_{3,3}\ F_{33} - F_{21}\ F_{12}\ u_{3,3}\ F_{33} + F_{11}\ F_{22} - F_{21}\ F_{12})\ u_{1,1} \\
&\quad + F_{22}\ u_{3,3}\ F_{33} + F_{22} \\
C_{33} &= (F_{11}\ u_{2,2}\ F_{22}\ F_{33} - u_{2,2}\ F_{21}\ F_{12}\ F_{33} + F_{11}\ F_{33})\ u_{1,1} \\
&\quad + u_{2,1}\ F_{12}\ F_{33} + u_{2,2}\ F_{22}\ F_{33} + u_{1,2}\ F_{21}\ u_{2,1}\ F_{12}\ F_{33} \\
&\quad - u_{2,1}\ F_{11}\ u_{1,2}\ F_{22}\ F_{33} + u_{1,2}\ F_{21}\ F_{33} + F_{33} \\
C_{12} &= (F_{21}\ F_{12}\ u_{3,3}\ F_{33} - F_{11}\ F_{22}\ u_{3,3}\ F_{33} + F_{21}\ F_{12} - F_{11}\ F_{22})\ u_{2,1} \\
&\quad + F_{21} + F_{21}\ u_{3,3}\ F_{33} \\
C_{21} &= (F_{21}\ F_{12}\ u_{3,3}\ F_{33} - F_{11}\ F_{22}\ u_{3,3}\ F_{33} + F_{21}\ F_{12} - F_{11}\ F_{22})\ u_{1,2} \\
&\quad + F_{12}\ u_{3,3}\ F_{33} + F_{12} \\
C_{13} &= 0 \qquad C_{31} = 0 \qquad C_{23} = 0 \qquad C_{32} = 0
\end{aligned}
$$

7 Simulation Results

Simulation results and error estimate calculations are presented in this section. Figure 6 illustrates the sequence of 2-D axisymmetric quadrilateral meshes used to model the problem and compute error estimates. A uniform mesh was used for the elastomer and steel directly beneath the region of highest intensity shock loading; the mesh was grown at 5% away from this region. As a measure of the element size, N=4, 6, 7, 9, 11, 12 and 13 elements were used across the thickness of the elastomer.

15
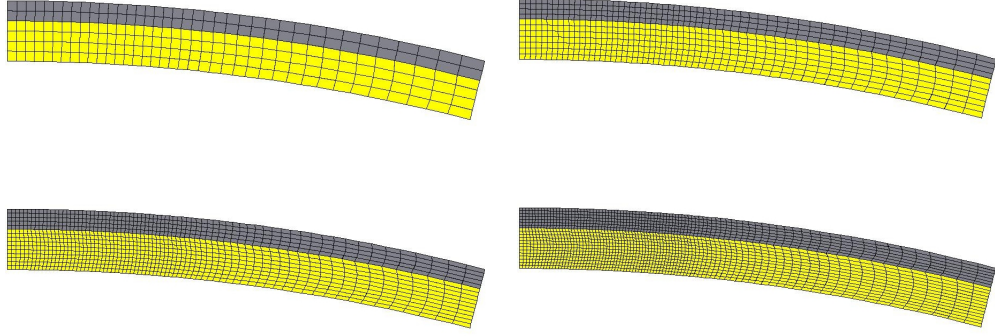
Figure 6. Meshes

7.1 _Primal Solution_ Figure 7 presents material plots of a simulation of the updated Lagrangian equations of motion using a Lagrangian mesh throughout the domain. The shell is composed entirely of steel and had no elastomeric layers; this may be considered the base model from which comparisons can be made between configurations that contain elastomeric layers. Figure 8 presents the predicted final stress state of the shell. Shown is deviatoric components of the stress, s_{rr}, s_{zz}, and s_{rz}, along with the pressure. The contours are given in units of Pascal's ranging from -650 MPa to +550 MPa. The standard sign convention is employed: tension positive, compression negative, and positive traction on positive element face is positive shear. The plots indicate that the loading is not localized beneath the region of highest intensity shock loading. Regions away from the centerline, including the far edge of the shell, experience large stress states. The contours shown are in units of Pascal's.
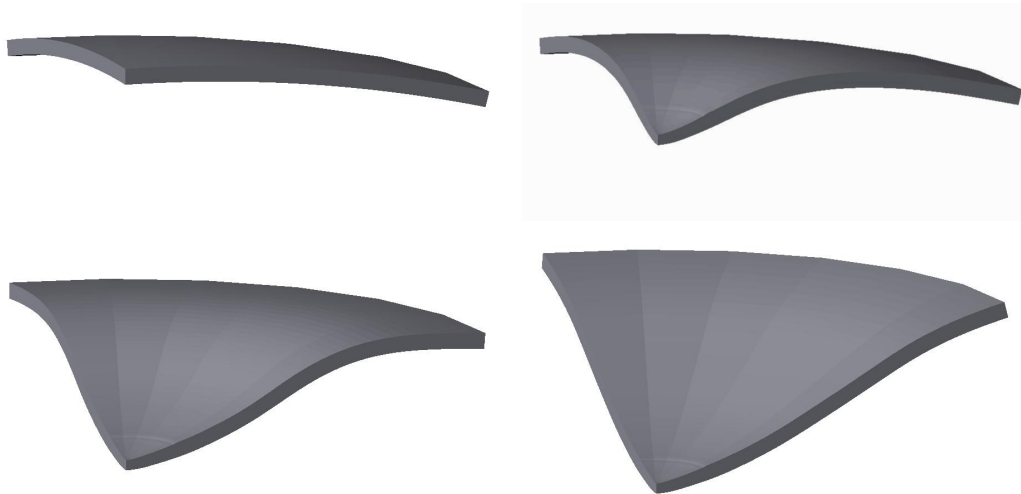
Figure 7. Results for Primal Problem. Base model. Steel only. top-left: t = 0 μs top-right: t = 100 μs bottom-left: t = 300 μs bottom-right: t = 500 μs

16
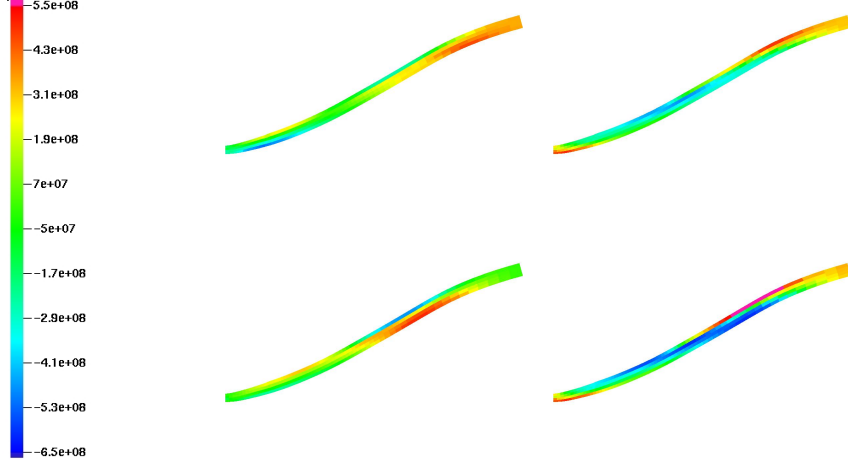
Figure 8. Final stress states. Base model. Steel only. top-left: s_{rr} top-right: s_{zz} bottom-left: s_{rz} bottom-right: pressure

Figure 9 presents material plots of a Lagrangian simulation with the configuration taken as steel on top, elastomer on bottom, and a sliding interface between the steel and elastomer. Figure 10 presents the predicted final stress state of the shell corresponding to Figure 9. The layers of the shell have separated near the centerline. Because of the separation one would expect a final stress state similar to the base model. However, the contact region near the outer edge of the shell appears to have mollified the regions of high shear stress but exacerbated the regions of high radial and axial stress along with the pressure.
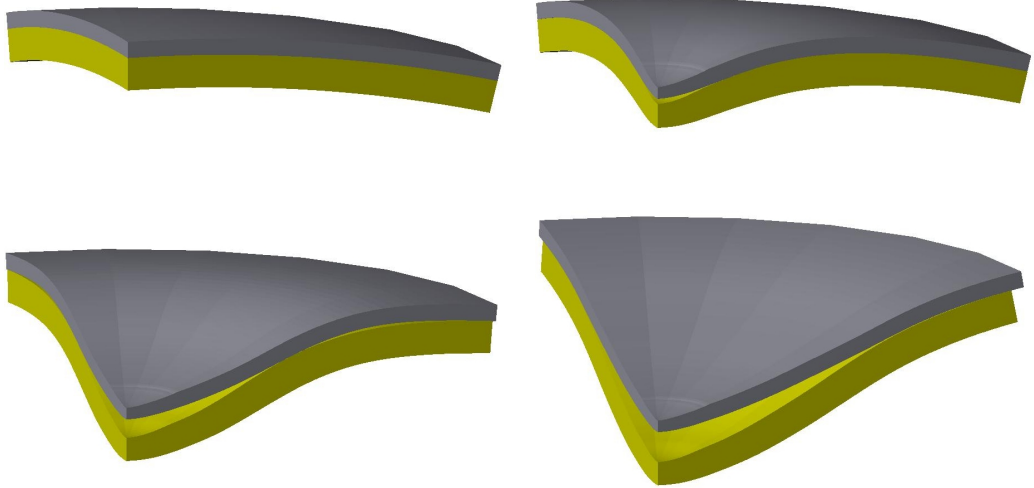
Figure 9. Steel layer on top. Sliding Interface top-left: t = 0 μs top-right: t = 100 μs bottom-left: t = 300 μs bottom-right: t = 500 μs

17
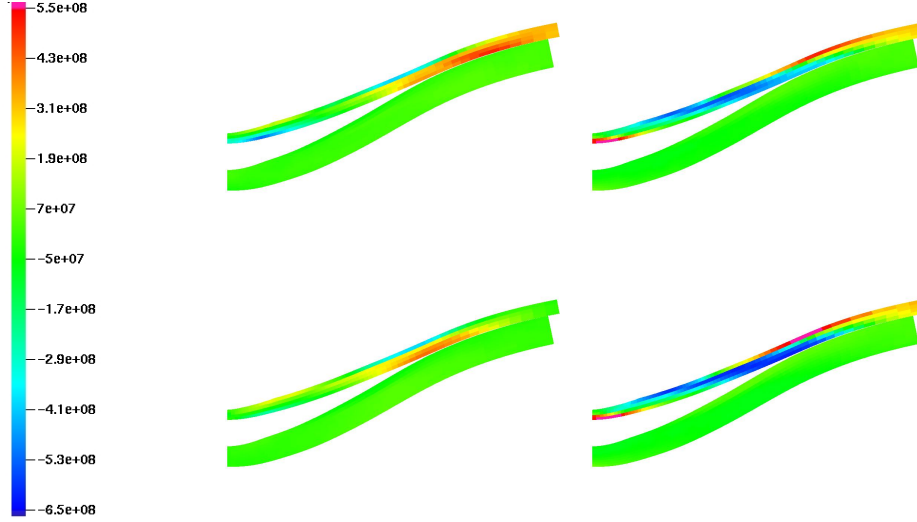
Figure 10. Results for Primal Problem. final stress states top-left: s_{rr} top-right: s_{zz} bottom-left: s_{rz} bottom-right: pressure

Results presented in Figure 11 are for the same configuration as those in Figure 9 except the interface between the steel and elastomer is modeled as perfectly bonded. The treatment of the interface condition between elastomer and steel is not seen to significantly affect the final deformed shape of the hull. However, Figure 12 shows that the final stress state has significantly changed. The loading absorbed by the steel directly under the region of highest intensity shock loading appears to be reduced and loading away from the centerline has increased.
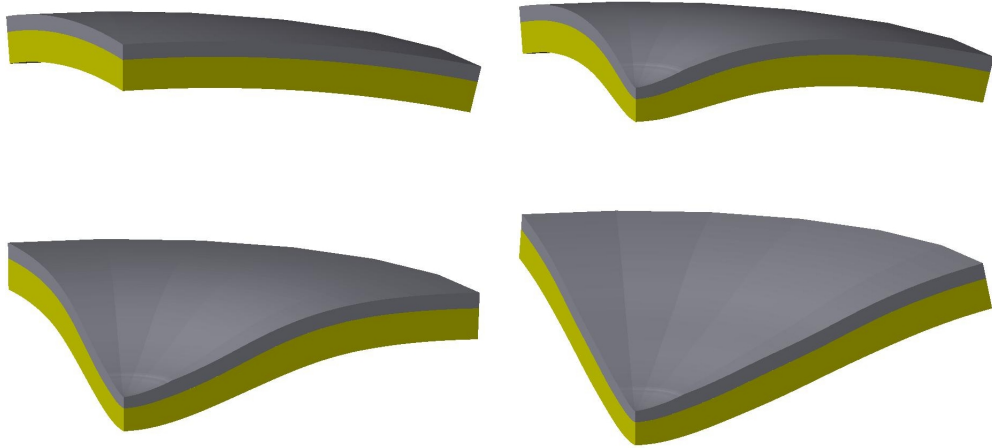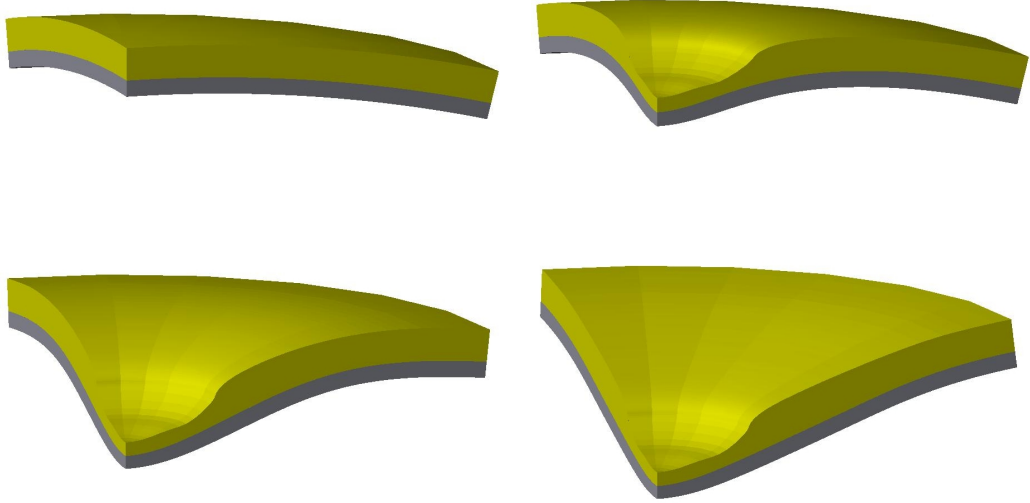

Figure 11. Steel layer on top. Bonded interface between steel and elastomer. top-left: t = 0 μs top-right: t = 100 μs bottom-left: t = 300 μs bottom-right: t = 500 μs

18
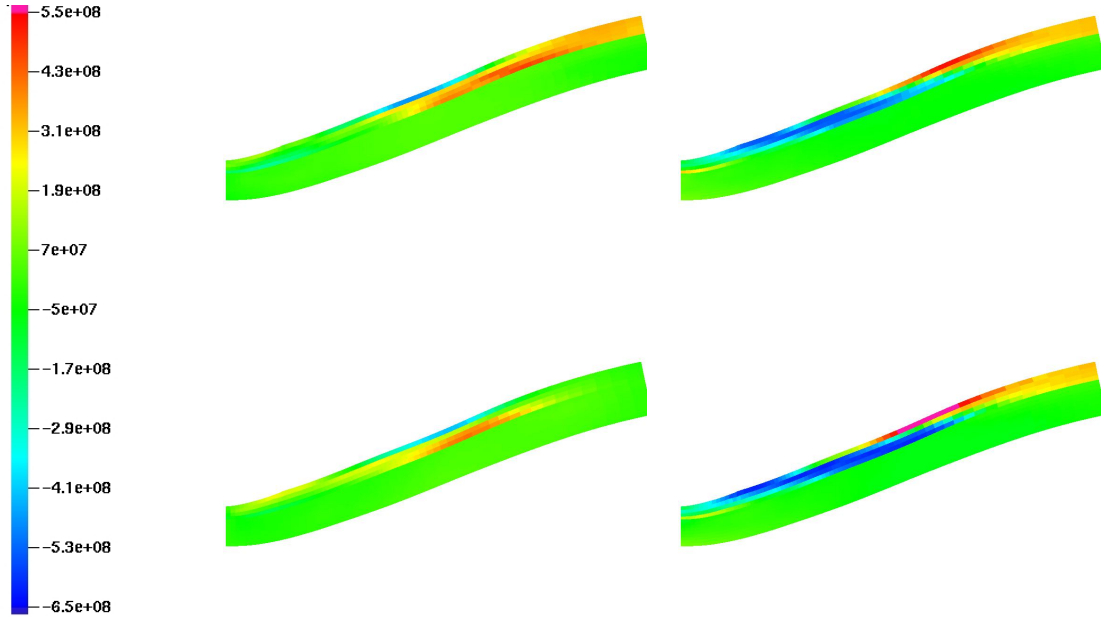
Figure 12. Steel Top. Perfectly Bonded. final stress states top-left: s_{rr} top-right: s_{zz} bottom-left: s_{rz} bottom-right: pressure

Figure 13 presents the calculations for the shell configuration with the elastomer on top of the steel. The interface between the steel and elastomeric layer is modeled as frictionless sliding. An onset of a pressure instability in the shell caused by the contact algorithm combined with the use of reduced integration is seen at time $t = 100$ μs. The stress state at late times, Figure 14, shows the effect of this instability. Simulations results away from the centerline are not as reliable as the results near the centerline.
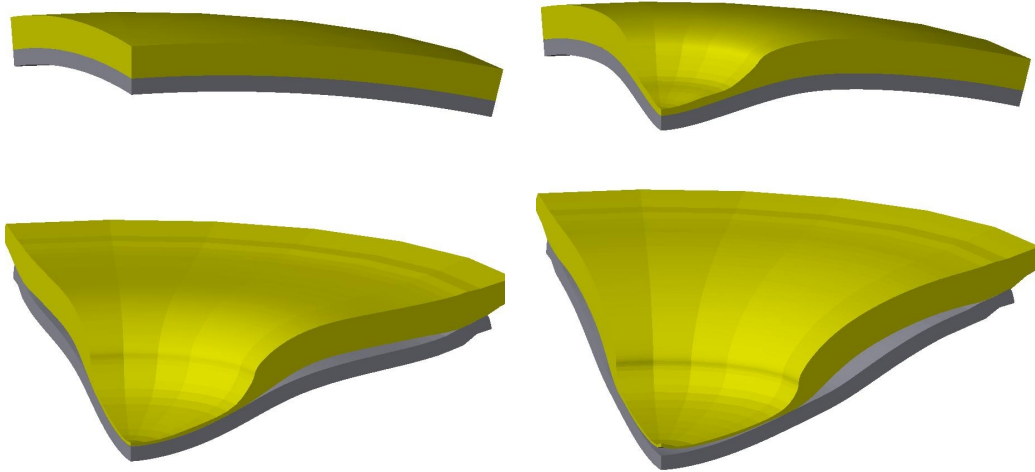
Figure 13. Elastomeric layer on top. Sliding interface between steel and elastomer. top-left: t = 0 μs top-right: t = 100 μs bottom-left: t = 300 μs bottom-right: t = 500 μs

19

Figure 14. Elastomeric layer on top. Sliding interface between steel and elastomer. final stress states top-left: s_{rr} top-right: s_{zz} bottom-left: s_{rz} bottom-right: pressure

The results from the layer configuration with the elastomer on top and the interface between the shell layers modeled as perfectly bonded are presented in Figure 15. Notice that the final stress state, Figure 16, is surprisingly similar to the stress state shown in Figure 12; indicating that the interface between the layered shell is more significant than the position of the layers.

Figure 15. Elastomeric layer on top. Bonded interface between steel and elastomer. top-left: t = 0 μs top-right: t = 100 μs bottom-left: t = 300 μs bottom-right: t = 500 μs
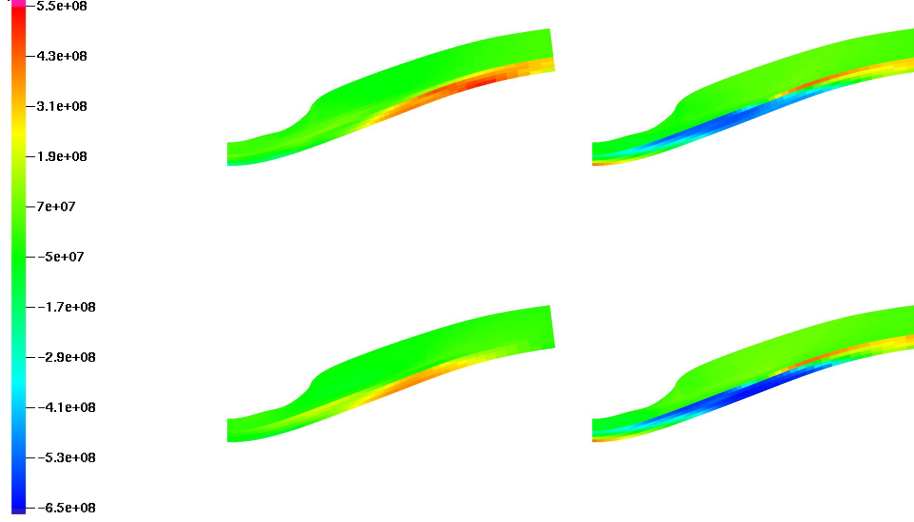
Figure 16. Results for Primal Problem. final stress states top-left: s_{rr} top-right: s_{zz} bottom-left: s_{rz} bottom-right: pressure

7.2   Dual Solution The dual solution corresponding to the results given in Figure 9, steel-on-top, sliding interface, are shown in Figures 17, 18, and 19. The specific quantity of interest is the displacement of a region of the elastomeric layer under the loading of the region of highest shock loading intensity. Figures 17 and 18 show the radial and axial components of the dual solution. Time $t = 90\mu s$ of the axial dual solution illustrates the position of the region used for the error computation. The magnitude of the axial component of the dual solution is seen to increase as the integration backwards in time proceeds.
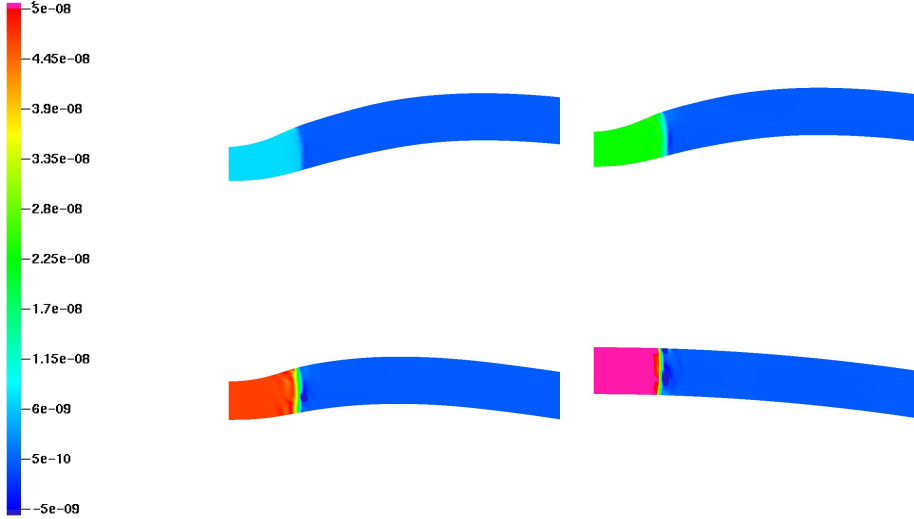
Figure 17. Axial Component of Dual Solution. Steel layer on top. Sliding interface. top-left: t = 90 μs top-right: t = 70 μs bottom-left: t = 40 μs bottom-right: t = 0 μs
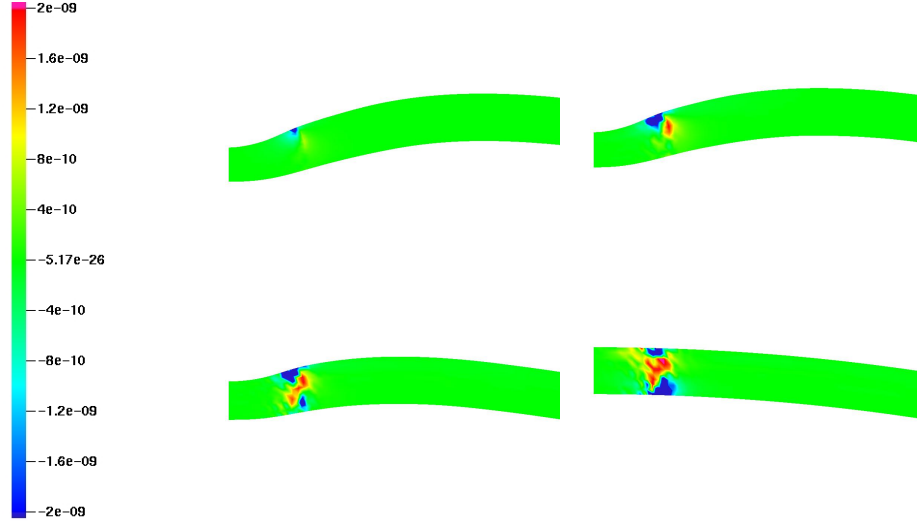
Figure 18. Radial Component of Dual Solution. Steel layer on top. Sliding interface. top-left: t = 90 μs top-right: t = 70 μs bottom-left: t = 40 μs bottom-right: t = 0 μs

The quantity of interest was chosen as the average displacement in the axial direction, consequently, the radial component of the dual solution is seen to be an order of magnitude smaller than the axial component. In terms of the final error estimate calculations, this means that forces and stresses affecting the radial momentum of the elastomer have a significantly less contribution to the final error estimate.
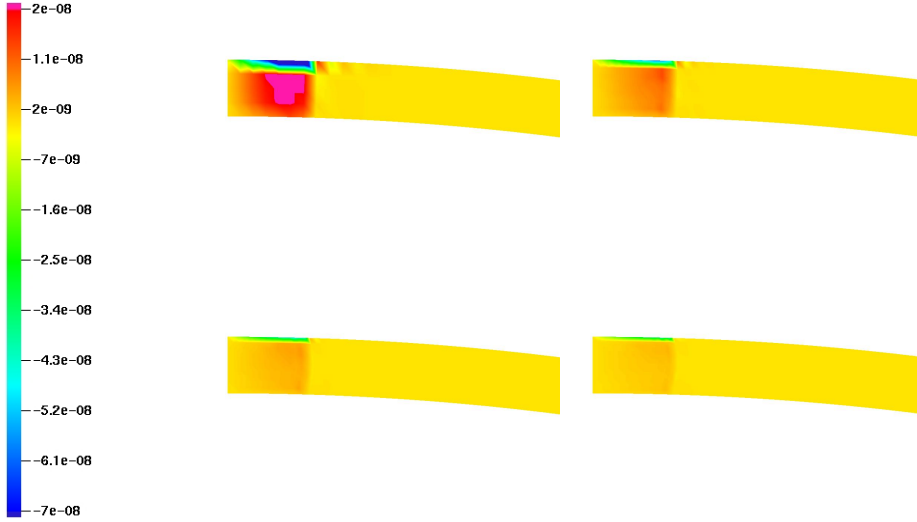
Figure 19. Spatial Distribution of Residual. Steel layer on top. Sliding interface. N= # of mesh cells across thickness of elastomer. top-left: $N = 6$, top-right: $N = 10$, bottom-left: $N = 14$, and bottom-right: $N = 18$

Figure 19 plots the spatial distribution of the contributions associated with each node over the entire time interval to the error in the quantity of interest

for different meshes. The region where the magnitude of these contributions is largest indicates where mesh refinement is needed. The regions close to the region of interest and near the highest intensity loading influence the quantity of interest the most. Thus mesh refinement only directly underneath the region of highest shock loading intensity is needed for accurate computations of the quantity of interest.
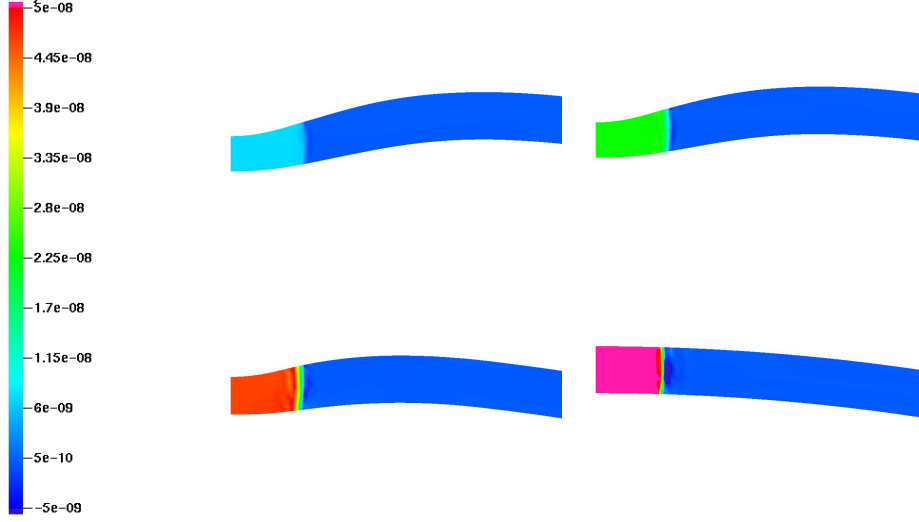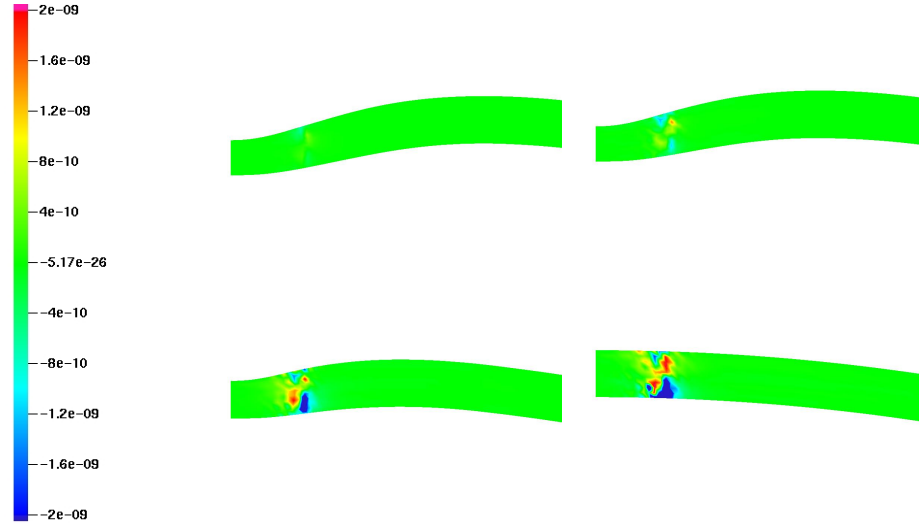

Figure 20. Axial Component of Dual Solution. Steel layer on top. Bonded interface. top-left: t = 90 μs top-right: t = 70 μs bottom-left: t = 40 μs bottom-right: t = 0 μs

Figure 21. Radial Component of Dual Solution. Steel layer on top. Bonded interface. top-left: t = 90 μs top-right: t = 70 μs bottom-left: t = 40 μs bottom-right: t = 0 μs

Figures 20, 21, and 22 illustrate the dual solution results corresponding to the steel-on-top configuration of the layered shell with a bonded interface between

the layers. Figures 20 and 21 are the axial and radial components of the dual solution. The results are similar to before. The regions near the quantity of interest and where the highest intensity loading originates require the most refinement. The majority of the error contributions are a consequence of the loading.
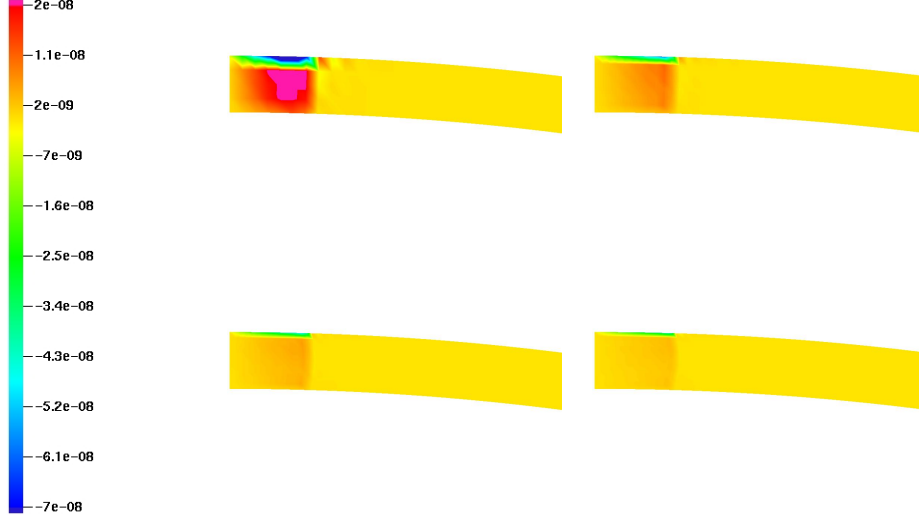

Figure 22. Spatial Distribution of Residual. Steel layer on top. Bonded interface. N= # of mesh cells across thickness of elastomer. top-left: $N = 6$ top-right: $N = 10$ bottom-left: $N = 14$ bottom-right: $N = 18$

Shown in Figure 23 is a graph of the global contributions in space at each time step to the error in the quantity of interest for both the sliding interface and bonded interface conditions. The time instances that contribute the most error
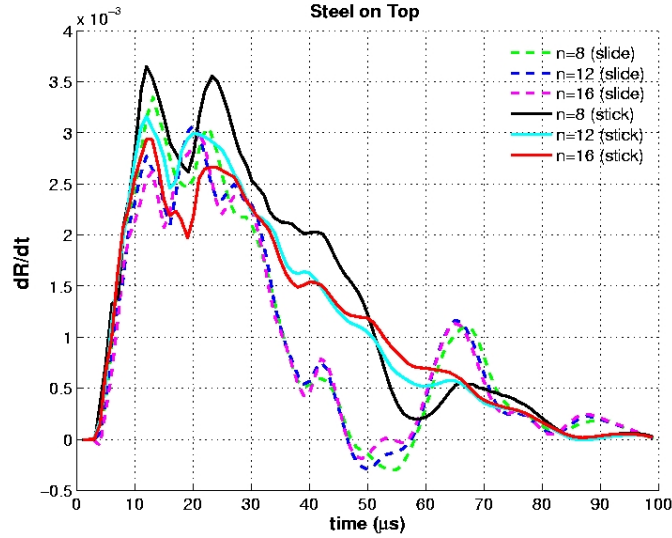
Figure 23. Temporal Distribution of Residual. Steel layer on top.

correspond to the loading of the elastomer by the pressure wave. Figure 24 plots the evolution of the final error estimates as a function of time.
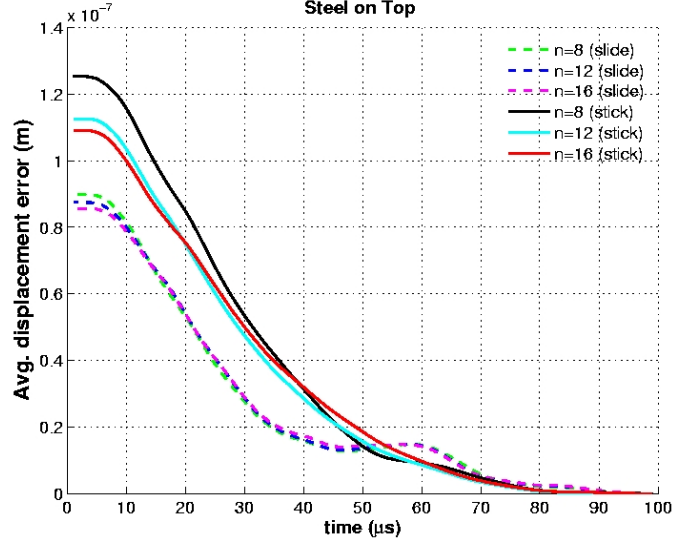
Figure 24. Temporal Evolution of Final Error Estimate. Steel layer on top.

Figures 25, 26, and 27 are the dual solution results corresponding to Figure 13, elastomer on top, sliding interface. The radial and axial components of the dual solution are shown in Figures 25 and 26. Note, for this case the dual solution was only computed for $T = 15$ μs. Large displacement gradients at late times
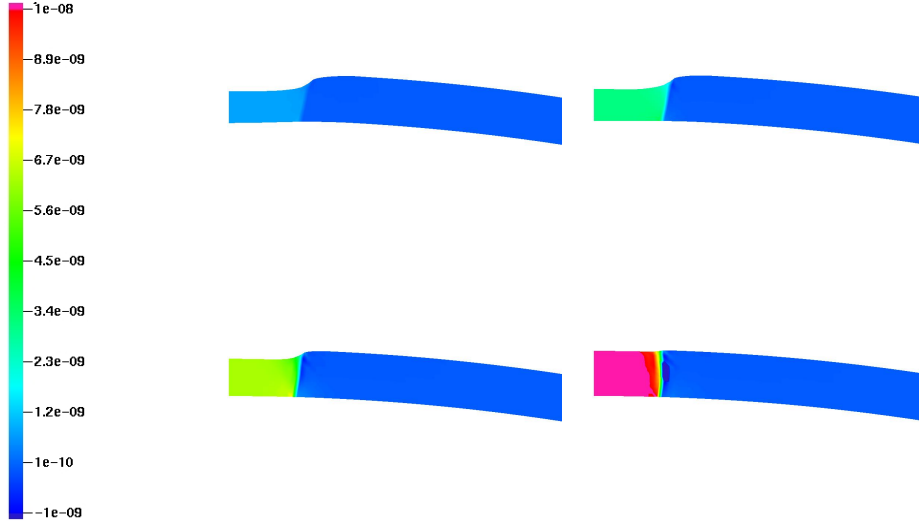

Figure 25. Axial Component of Dual Solution. Elastomeric layer on top. Sliding interface. top-left: t = 13 μs top-right: t = 10 μs bottom-left: t = 7 μs bottom-right: t = 1 μs

cause numerical instabilities in the dual solution and are the cause of the time interval restriction. However, the results are similar to those obtained before. The regions in the mesh where the highest intensity structural loading originates require the most refinement and the residual is seen to significantly increase for higher mesh resolutions.
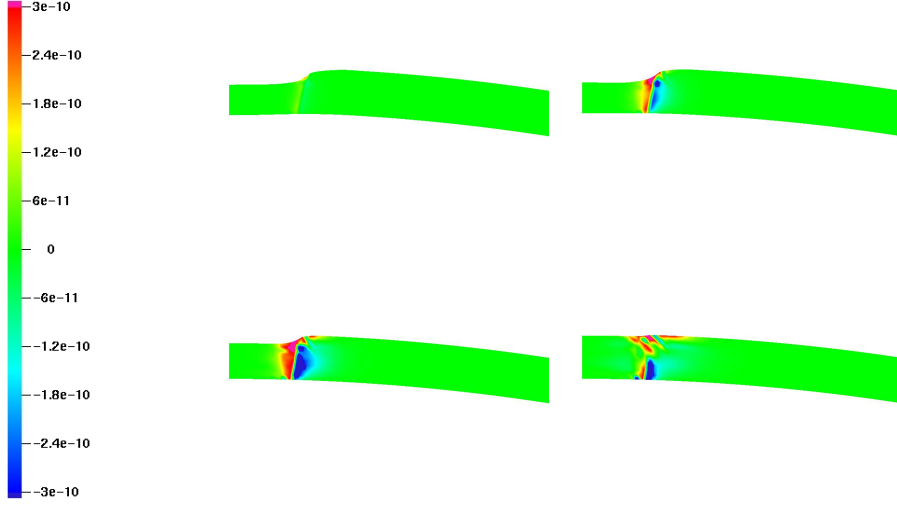
Figure 26. Radial Component of Dual Solution. Elastomeric layer on top. Sliding interface. top-left: t = 13 μs top-right: t = 10 μs bottom-left: t = 7 μs bottom-right: t = 1 μs
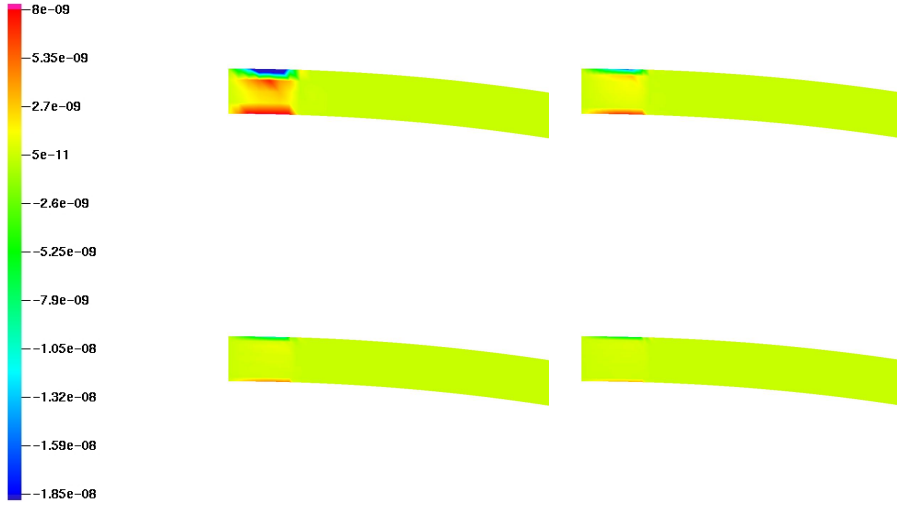

Figure 27. Spatial Distribution of Residual. Elastomeric layer on top. Sliding interface. N= # of mesh cells across thickness of elastomer. top-left: $N = 6$ top-right: $N = 10$ bottom-left: $N = 14$ bottom-right: $N = 18$

The dual solution results corresponding to Figure 15, elastomer on top, bonded interface, are shown in Figures 28, 29, and 30. The radial and axial components of the dual solution are shown in Figures 28 and 29. Again, the dual solution was only computed for $T = 15$ μs. The results are consistent; the axial component of the dual solution is an order of magnitude larger than the radial component and regions in the mesh where the highest intensity structural loading originates contribute significantly to the error.
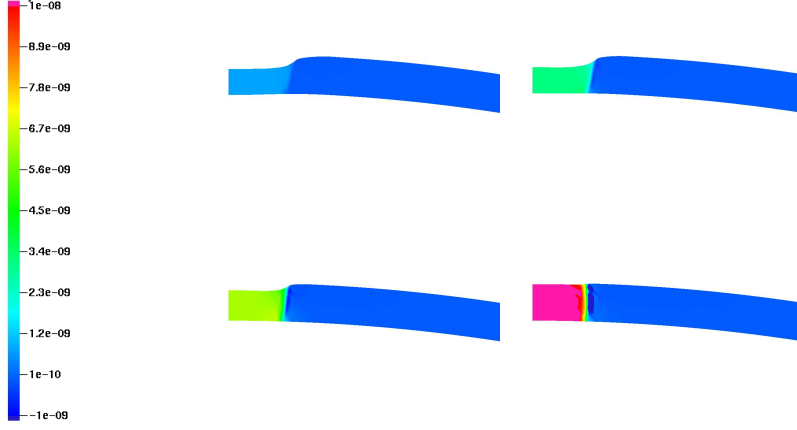
Figure 28. Axial Component of Dual Solution. Elastomeric layer on top. Bonded interface. top-left: t = 13 μs top-right: t = 10 μs bottom-left: t = 7 μs bottom-right: t = 1 μs
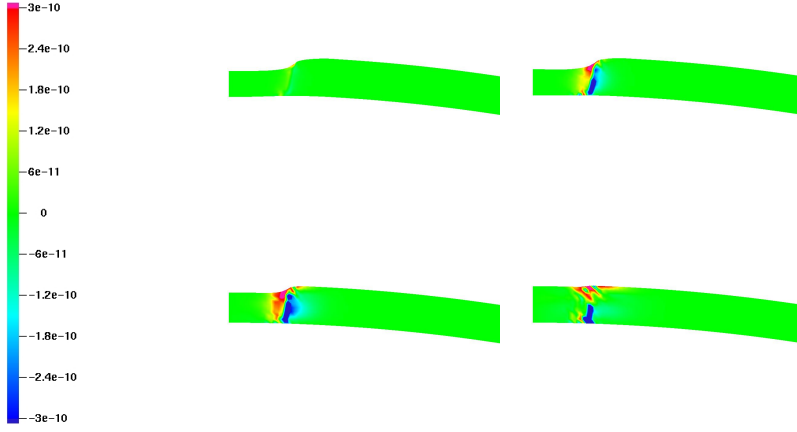

Figure 29. Radial Component of Dual Solution. Elastomeric layer on top. Bonded interface. top-left: t = 13 μs top-right: t = 10 μs bottom-left: t = 7 μs bottom-right: t = 1 μs
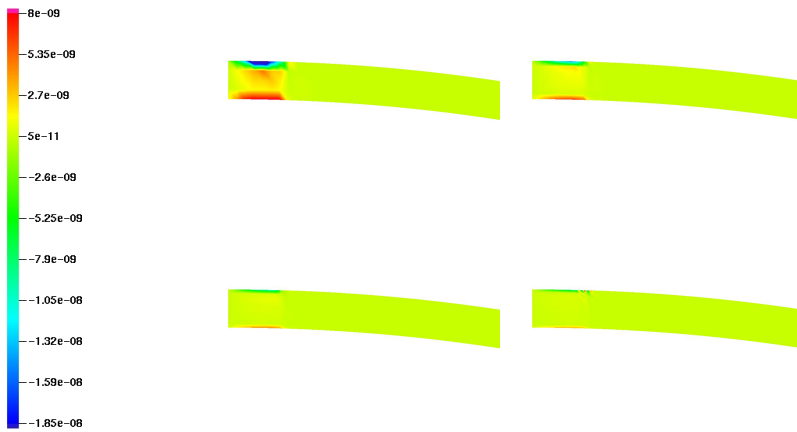

Figure 30. Spatial Distribution of Residual. Elastomeric layer on top. Bonded interface. N= # of mesh cells across thickness of elastomer. top-left: $N = 6$ top-right: $N = 10$ bottom-left: $N = 14$ bottom-right: $N = 18$

The temporal contributions to the residuals as a function of time for both sliding and bonded interface conditions are shown in Figures 31 and 32. For this short time interval the quantity of interest is seen to being highly effected by the loading throughout the duration of the simulation.
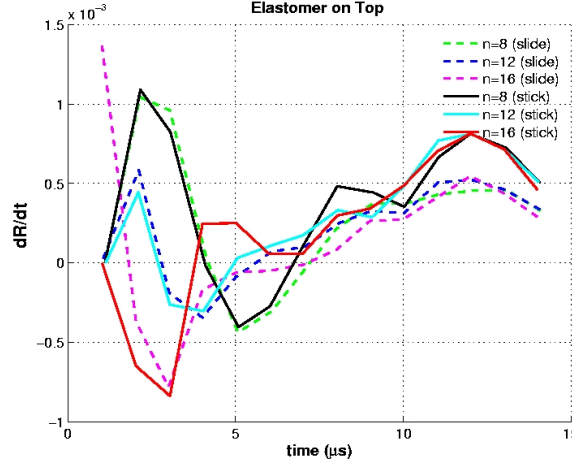

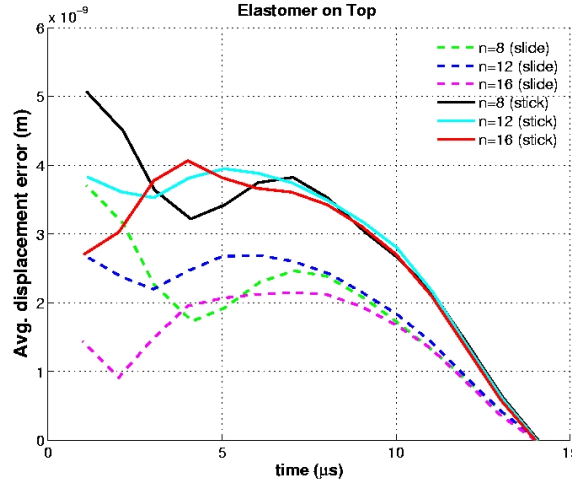Figure 31. Temporal Distribution of Residual. Elastomeric layer on top.

Figure 32. Temporal Evolution of Final Error Estimate. Elastomeric layer on top.

Figures 33 and 34 show final error estimates corresponding to equation (20). The error estimate is plotted against the number of degrees of freedom in the mesh. As expected the error estimates are seen to decrease with mesh resolution and the error estimates for the configuration with elastomer on top is seen to have less accumulation of error because of the shorter time interval that the problem was run on.

The interface condition between the steel and elastomer for the configuration with steel on top is seen to produce a substantial difference in the rates of convergence. This may be attributed to the difference in the loading of the elastomer. For the configuration with elastomer on top, the rates of convergence are roughly the same for both interface conditions. Over the short time

28

interval in which error estimates were computed the initial loading for both interface conditions is approximately the same.
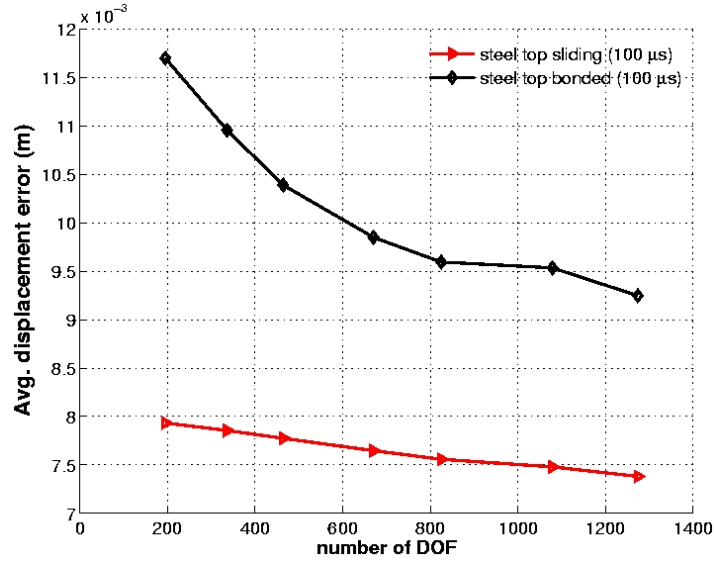

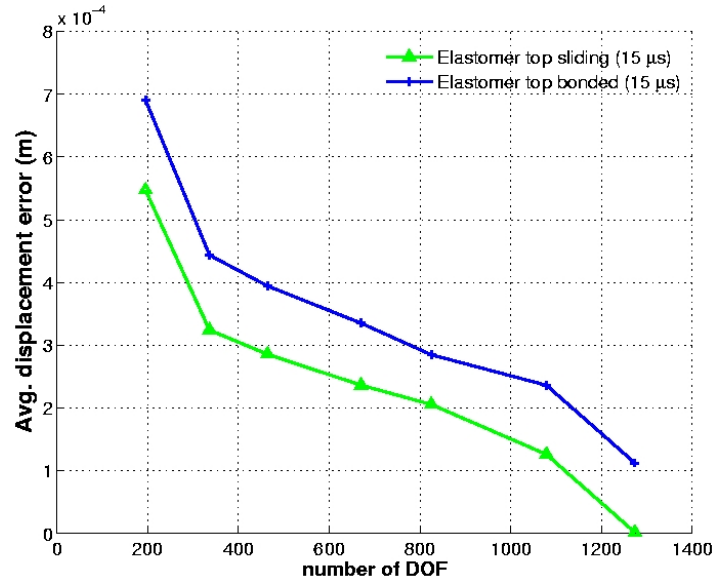Figure 33. Estimate Error as a function of number of degrees of freedom. Steel layer on top.

Figure 34. Estimated Error as a function of number of degrees of freedom. Elastomeric layer on top.

8   Conclusions

In summary, a new simulation tool has been developed to study nonlinear dynamics and large deformations of shock-loaded structures. The theory of goal oriented error estimation has been applied to a class of highly nonlinear shock loaded problems. Material properties of the elastomer were exploited, allowing

approximations to the Cauchy stress, resulting in a computationally feasible dual problem for highly complex phenomena. The dual solution was used to obtain converging error estimates for a meaningful quantity of interest. This work may be used as a foundation for developing adaptive meshing algorithms for this class of nonlinear problems.

In this study, extensive numerical calculations were performed on various configurations of layered-shell structures. The primary effect of the elastomer was to redistribute the regions of high stress concentration through out the steel. Results also showed that the differences in the final stress state, as compared to the base model, is dominated by the interface between the layers of the shell; i.e. the positions of the layer is not significant, but the mechanism that allows the transfer of energy and momentum between the layers is very important.

References

[1] M. Ainsworth and J.T. Oden. *A Posteriori Error Estimation in Finite Element Analysis.* John Wiley & Sons, New York, 2000.

[2] J.H. Argyris. Continua and discontinua. In *Proceedings of the Conference on Matrix Methods in Structural Mechanics*, volume AFFDL-TR-66-80, Ohio, October 1965. Wright-Patterson AFB.

[3] I. Babuška and W.C. Rheinboldt. A posteriori error estimates for the finite element method. *Internat. J. Numer. Methods Engrg.*, 12:1597–1615, 1978.

[4] I. Babuška, O.C. Zieniewicz, J. Gago, and E.A. Oliveira, editors. *Accuracy Estimates and Adaptive Refinements in Finite Element Computations.* John Wiley & Sons, N.Y., 1986.

[5] R.E. Bank and A. Weiser. Some a posteriori error estimates for elliptic partial differential equations. *Math. Comp.*, 44:283–301, 1985.

[6] R. Becker and R. Rannacher. An optimal control approach to a posteriori error estimation in finite element methods. *Acta Numerica*, 10:1–102, 2001.

[7] T. Belytschko, W. Liu, and B. Moran. *Nonlinear Finite Elements for Continua and Structures.* John Wiley and Sons, Hoboken, 2000.

[8] T.D. Blacker and M.B. Stephenson. Paving: A new approach to automated quadrilateral mesh generation. *Inter. J. for Numer. Methods in Engng.*, 32:811–847, 1991.

[9] W. M. Deen. *Analysis of Transport Phenomena*. Oxford University Press, New York, 1998.

[10] E.C. Gartland. Computable pointwise error bounds and the ritz method in one dimension. *Siam J. Numer. Anal.*, 21:84–100, 1984.

[11] M.E. Gurtin. *An Introduction to Continuum Mechanics*. Academic Press, San Diego, 1981.

[12] P. Ladevèze. *Comparaison de modèles de milieux continus.* PhD thesis, Université P. et M. Curie, Paris, 1975.

[13] J. McGee, J. Isaacs, and S. Nemat-Nasser. Quick look: Constitutive model for polyurea at large compressive strains and high strain rates. Technical report, University of California San Diego, 2004.

[14] J.T. Oden. *Finite Elements of Nonlinear Continua*. Mcgraw-Hill, N.Y., 1972.

[15] J.T. Oden and L.F. Demkowicz. Advances in adaptive improvements: A survey of adaptive finite element methods in computational mechanics. In I. Babuška, O.C. Zieniewicz, J. Gago, and E.A. Oliveira, editors, *Accuracy Estimates and Adaptive Refinements in Finite Element Computations*. John Wiley & Sons, N.Y., October 1986.

[16] J.T. Oden and S. Prudhomme. Goal-oriented error estimation and adaptivity for the finite element method. *Computers and Mathematics with Applications*, 41:735–756, 2001.

[17] J.T. Oden and S. Prudhomme. Estimation of modeling error in computational mechanics. *Journal of Computational Physics*, 182:496–515, 2002.

[18] J.T. Oden, S. Prudhomme, A. Romkes, and P. Bauman. Multi-scale modeling of physical phenomena: adaptive control of models. *Submitted to Siam Journal on Scientific Computing*, 2005.

[19] J.T. Oden and K. Vemaganti. Estimation of local modeling error and goal-oriented modeling of heterogeneous materials: part i. *Journal of Computational Physics*, 167:22–47, 2000.

[20] D. Pardo, L. Demkowicz, C. Torres-Verdin, and M. Paszynski. A self-adaptive goal oriented hp-finite element method with electromagnetic applications. part ii: Electrodynamics. *Submitted to SIAM Journal on Applied Mathematics*, 2005.

[21] A. Romkes and J.T. Oden. Adaptive modeling of wave propagation in heterogeneous elastic solids. *Comput. Methods Appl. Mech. Engng.*, 193:1603–1632, 2004.

[22] K. Vemaganti and J.T. Oden. Estimation of local modeling error and goal-oriented modeling of heterogeneous materials; part ii: A computational environment for adaptive modeling of heterogeneous elastic solids. *Comput. Methods Appl. Mech. Engng.*, 190:6089–6124, 2001.

[23] R. Verfürth. *A review of a posteriori error estimation and adaptive mesh refinement techniques.* Wiley-Teubner, 1996.